Optical properties of single-crystal $Sr_2CuO_2Cl_2$

A. Zibold, H. L. Liu, S. W. Moore, J. M. Graybeal, and D. B. Tanner
Department of Physics, University of Florida, Gainesville, Florida 32611
(Received 8 November 1995)

We report reflectance measurements of single-crystal $Sr_2CuO_2Cl_2$ over the frequency range between 30 cm^{-1} and 40 000 cm^{-1}. Using crystals of 10 μm to 100 μm thickness we were also able to perform transmittance measurements at frequencies below the lowest phonon mode as well as between the highest phonon mode and the charge-transfer gap. The measurements were done on the (001) surface with ab polarization at temperatures between 10 K to 360 K. With decreasing temperature the phonon modes shift to higher frequencies; the 340 cm^{-1} stretching mode splits below 300 K. The most notable feature in the transmittance spectrum is a weak electronic absorption, possibly magnetic in origin. This feature is not resolved in the reflectance. At the charge-transfer gap there is an increase in the conductivity by four orders of magnitude. The charge-transfer gap energy increases with decreasing temperatures. In addition there is a temperature-dependent absorption band in the low-frequency tail of the fundamental absorption edge.

I. INTRODUCTION

A common feature of cuprate materials is the presence of a metal-insulator transition, with a change from a conducting, often superconducting, phase into a quasi-two-dimensional antiferromagnetic phase as the mobile charges are removed. These insulating ''parent'' compounds of the cuprate superconductors are charge-transfer insulators, with an energy gap between 1.5 eV (12 000 cm^{-1}) and 2.0 eV (16 000 cm^{-1}). Detailed studies of these insulators are interesting, because a variety of different absorption processes, like phonons, antiferromagnetism, and defects, which may play a key role for superconductivity in the conducting phase, can be directly investigated.

Previous optical reflectance studies on single crystals have concentrated on the metal-insulator transition[1–4] and the light doping regime[5] in $La_{2-x}Sr_xCuO_4$, $Nd_{2-x}Ce_xCuO_4$, and $YBa_2Cu_3O_{6+x}$. In the undoped phase, studies of phonon properties in the low-energy range [far infrared (FIR)] and of interband transitions in the high-energy range (above 10 000 cm^{-1}) have been performed on a variety of materials.[6–12] Whereas the reflectance spectra of the insulating ''parent'' compounds are almost constant between the highest phonon frequency and the charge-transfer gap, recent midinfrared transmittance measurements on thin platelets reveal a variety of interesting features within the gap.[13–16]

In this paper we report the optical properties of $Sr_2CuO_2Cl_2$ obtained on samples with different thicknesses (26 μm, 50 μm, and 100 μm). The measurements have been performed on the (001) surface, representing the in-plane excitations in the material. Whereas the reflectance ($\mathscr{R}$) can be measured over a wide frequency range, transmittance ($\mathscr{T}$) measurements can only be made in regions of weak absorption ($\alpha < 1000$ cm^{-1}). In energy ranges where the extinction coefficient ($k = c\alpha/2\omega$) is, for example, below 0.1 and the refractive index (n) is higher than 1.5, the reflectance has a change of $< 0.5\%$ as k changes by a factor of 2. In these limits, reflectance measurements are insensitive to changes in k. In contrast the measurement of $\mathscr{T}$ for a sample with suitable thickness ($\alpha d < 5$) is a sensitive tool to investigate k.

II. EXPERIMENTAL DETAILS

A. Sample growth and structure

The single crystals were grown as described by Miller *et al.*[17] by melting prereacted $Sr_2CuO_2Cl_2$. This method yields thin platelets with fairly large (001) surfaces. The material is a single-layered perovskite which has structural similarities to the La_2CuO_4 compound. At high temperature both materials have a tetragonal K_2NiF_4 structure, but, unlike La_2CuO_4, no orthorhombic distortion has been reported for $Sr_2CuO_2Cl_2$ at low temperatures. The Cu-O planes, perpendicular to the c axis, are stacked between Sr-Cl planes instead of between La-O planes. Therefore there are no apical oxygens in the $Sr_2CuO_2Cl_2$; instead there are apical chlorines. The $Sr_2CuO_2Cl_2$ is stoichiometric as grown. Vaknin *et al.*[18] report from neutron diffraction that the tetragonal structure exists down to at least 10 K. Magnetic susceptibility and neutron measurements show this material corresponds to a two-dimensional (2D) spin-1/2 Heisenberg antiferromagnet.[17,18] The spins are lying in the Cu-O planes. The Néel temperature is reported to be about $T_N \approx 250$ K, and the in-plane Cu-Cu exchange interaction constant J is about 900 K. Further results of ^{35}Cl nuclear spin-lattice relaxation rate measurements[19] and neutron scattering data[20] suggest a crossover below the Néel temperature to a 2D XY behavior, indicating a tiny in-plane anisotropy.[21]

B. Reflectance and transmittance measurements

The reflectance measurements were performed over a wide frequency region between 30 cm^{-1} and 40 000 cm^{-1} using three spectrometers with a variety of exchangeable components for different overlapping frequency ranges. The far-infrared and mid-infrared regions (30 cm^{-1}–3000 cm^{-1}) were measured using a Bruker IFS-113v fast scanning Fourier transform spectrometer. At higher frequencies

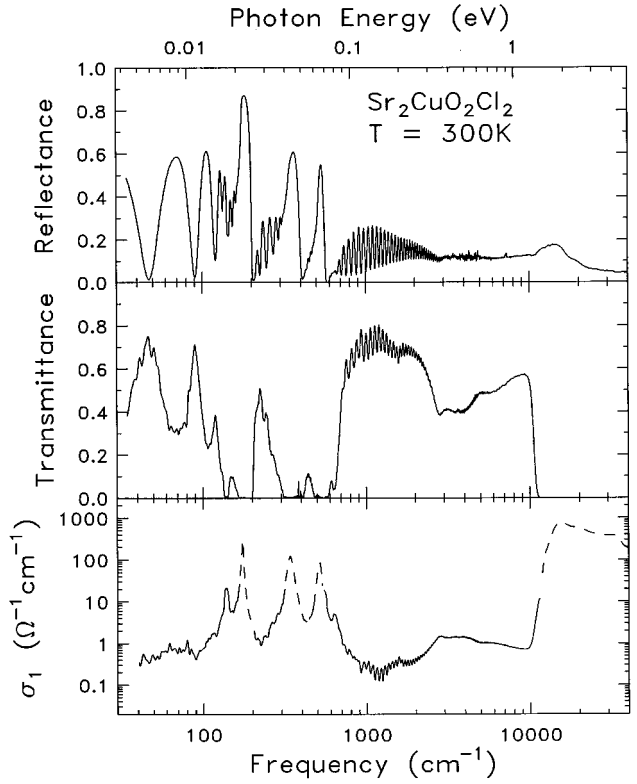

FIG. 1. The upper part of the panel shows the reflectance spectrum ($\mathscr{R}$) of a 26 μm thick $Sr_2CuO_2Cl_2$ sample at $T=300$ K. In the middle part the transmittance spectrum ($\mathscr{T}$) of the same sample is plotted. The lower panel shows the real part of the optical conductivity function (σ_1) determined by $\mathscr{R}$ and $\mathscr{T}$ (solid line) and by Kramers-Kronig analysis (dashed line).

(800 cm^{-1}–40 000 cm^{-1}) we obtained our spectra with a Perkin-Elmer 16 U grating spectrometer. The temperature of the sample was varied by using a helium-cooled flow cryostat with a silicon thermometer and a resistive heater. The investigated temperature range covered 10–360 K. The sample sizes for the measurements were about 2 mm in diameter. Although the samples had been either freshly cleaved or etched in 1% bromine in ethanol solution before the measurement, there is a frequency-dependent correction of the reflectivity in the visible and UV necessary due to the surface roughness. Therefore we did following procedure. At high frequencies (11 000 cm^{-1} – 40 000 cm^{-1}) the room temperature spectrum was compared to a reflectance spectrum measured with a MPM 800 Microscope Photometer with grating monochrometers, especially designed for spot measurements. Using a magnification of 10× and 20× we measured on shiny, smooth, and well-reflecting spots with a size about 50 μm × 50 μm. The structureless ratio of the spectra was used to correct the measured temperature-dependent spectra.

Figure 1 (upper panel) shows the reflectance for a 26 μm thick sample at 300 K. Note that the frequency is plotted on a logarithmic scale. Between the strong absorption features, the reflectance is dominated by fringes, which can be clearly seen in the far infrared and midinfrared. In these regions multiple internal reflections are present and finite transmittance of the sample can be expected. Deviations from the periodic modulation of the fringes indicate the presence of weak absorption processes. Whereas the reflectance was measured over the whole frequency range, the transmittance could be measured only up to about 12 000 cm^{-1}. Figure 1 (middle panel) shows the transmittance at 300 K of the same sample, which was measured in reflectance. In the far infrared and midinfrared fringes can be seen again. The maxima of the fringes in reflectance correspond to minima in transmittance and vice versa.

C. Determination of optical properties

The measured reflectance $\mathscr{R}(\omega)$ and transmittance spectra $\mathscr{T}(\omega)$ have been used to extract the complex dielectric function $\tilde{\epsilon}(\omega)=\epsilon_1(\omega)+\epsilon_2(\omega)$, the real part of the optical conductivity $\sigma_1(\omega)=\epsilon_0\omega\epsilon_2(\omega)$, the absorption coefficient $\alpha(\omega)$, and the loss function $\mathrm{Im}(-1/\tilde{\epsilon})=-\epsilon_2(\omega)/[\epsilon_1^2(\omega)+\epsilon_2^2(\omega)]$. Because our samples are transparent and show strong fringes from multiple internal reflections, the analysis is rather involved. Kramers-Kronig analysis requires a single-bounce reflectance spectrum $R_s(\omega)$ over a broad frequency region, along with suitable low- and high-frequency extrapolations. That $\mathscr{T}(\omega)\neq 0$ implies $\mathscr{R}(\omega)\neq R_s(\omega)$; when the sample is transparent, the reflectance includes a contribution from the rear surface. From $\mathscr{R}(\omega)$ and $\mathscr{T}(\omega)$, however, a solution for the optical properties can be either approximately or numerically found for each data pair at a single measured frequency. In this work we use an approximation solution, carried out as described below. For $T=300$ K we also obtained results with numerical extraction and found equivalent results using the approximation. Finally, for the discussion of the phonons we performed a fit of the conductivity function using a set of Lorentzian oscillators.

The analysis is done in the following way. The complex transmittance is given by

$$\tilde{t}(\omega)=\sqrt{\mathscr{T}(\omega)}\exp[i\Phi_t(\omega)]=\frac{\tilde{a}(1-\tilde{r}^2)}{(1-\tilde{a}^2\tilde{r}^2)}, \tag{1}$$

with

$$\tilde{a}=\exp(i2\pi\overline{\nu}\tilde{n}d) \tag{2}$$

and

$$\tilde{r}=\frac{\tilde{n}-1}{\tilde{n}+1}=\sqrt{R_s(\omega)}\exp[i\Phi_r(\omega)]. \tag{3}$$

Here d is the sample thickness in cm, $\overline{\nu}$ is the frequency in wave numbers (cm^{-1}), and $\tilde{n}=n+ik$ is the complex refractive index. By averaging over the phase, and in the limit $n\gg k$, which is a reasonable assumption as we will see below, the transmittance can be written[22]

$$\mathscr{T}(\omega)=\frac{A(\omega)[1-R_s(\omega)]^2}{1-A^2(\omega)R_s^2(\omega)}, \tag{4}$$

where

$$A(\omega)=\tilde{a}^*\tilde{a}=\exp(-4\pi\overline{\nu}kd). \tag{5}$$

With the approximation

$$R_s(\omega) \approx \frac{(n-1)^2}{(n+1)^2}, \tag{6}$$

the real and imaginary parts of the refractive index or dielectric function can be found as a function of $\mathscr{T}$, d, and R_s. Either the single-bounce reflectivity R_s must be measured on a thick sample with no transmittance or n must be extracted numerically as described next.

In the case of the numerical method we used for the measured reflectance $\mathscr{R}(\omega)$ the equation[23]

$$\mathscr{R}(\omega) = R_s(\omega)[.\mathscr{T}(\omega)A(\omega)+1]. \tag{7}$$

$\mathscr{R}(\omega)$ and $\mathscr{T}(\omega)$ are inverted to find $R_s(\omega)$ and $A(\omega)$ by iteration, assuming the first data point gives $A = 1$. The real and imaginary parts of the dielectric function can now be solved analytically.

Having the dielectric function we can calculate $R_s(\omega)$ in regions where $\mathscr{T}(\omega) \neq 0$. These data are combined with the measured $R_s(\omega)$ in regions of no transmittance, yielding the single-bounce reflectance over the whole spectral region. On this spectrum $R_s(\omega)$ we performed a Kramers-Kronig analysis to obtain the dielectric function. The low-frequency extrapolation below 30 cm^{-1} was chosen to be constant. For the high-frequency extrapolation we used between 5 eV and 40 eV published data of Tajima *et al.*[10] for isostructural materials, and after doing so we have assumed a free electron asymptotic behavior $\mathscr{R}(\omega) \propto \omega^{-4}$.

III. RESULTS AND DISCUSSION

A. Optical properties: Overall

In Fig. 1, lowest panel, we show the 300 K optical conductivity $\sigma_1(\omega)$ extracted from the two spectra shown in the upper panels. The solid line is obtained by solving from $\mathscr{R}(\omega)$ and $\mathscr{T}(\omega)$. The dashed line shows the part included from the Kramers-Kronig analysis. A good match is achieved. Below 100 cm^{-1} and between 1000 and 3000 cm^{-1} a few remaining fringes can be seen due to the slightly different angle of incidence used in the $\mathscr{R}(\omega)$ and the $\mathscr{T}(\omega)$ measurements. In both the low-frequency (phonons) and the high-frequency (interband) regions, conductivity reaches up to 800 $\Omega^{-1}\,cm^{-1}$, whereas the conductivity drops below 2 $\Omega^{-1}\,cm^{-1}$ in regions of significant transmittance.

The real and imaginary parts of the 300 K dielectric function are plotted in Fig. 2. The upper panel shows $\epsilon_1(\omega)$ and the lower panel $\epsilon_2(\omega)$. In the inset the interband region is plotted in an expanded scale. The analysis reveals strong changes in $\tilde{\epsilon}$ for the four phonon modes, especially for the 173 cm^{-1} vibration. An assignment and a detailed discussion of the phonon modes will be given in the next section. In the midinfrared, a flat $\epsilon_1(\omega)$ can be seen and gives $\epsilon_1 \approx 3.5$, consistent with earlier reports.[13] As long we have high transmittance in our material and therefore $\epsilon_1(\omega) \approx n^2$ this indicates a mainly constant refractive index n in this range. Finally, the charge-transfer structure comes at high frequency. Figure 3 shows the absorption coefficient over the whole frequency region at room temperature. The behavior is similar to the conductivity. The interruption of the curve is due to the change of the data extraction from the $\mathscr{R}(\omega)$, $\mathscr{T}(\omega)$ solution to the Kramers-Kronig result.

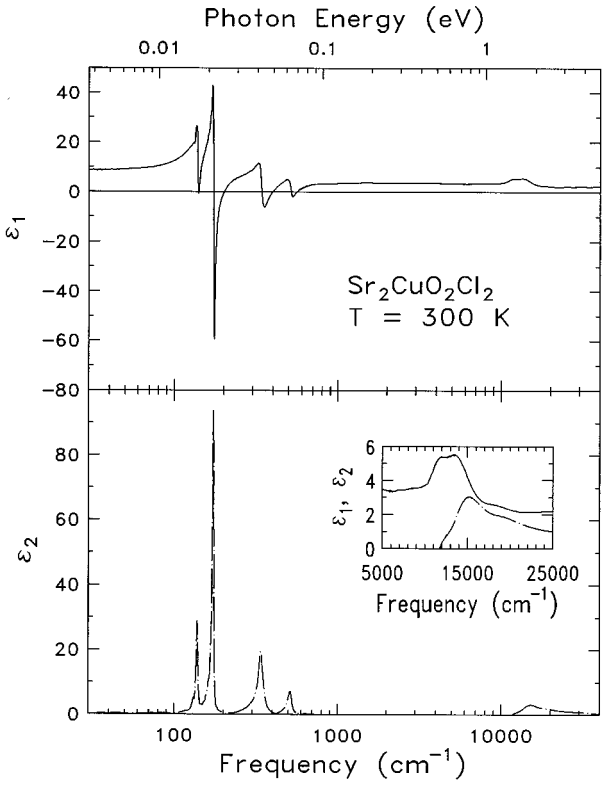

FIG. 2. The real part $\epsilon_1(\omega)$ (upper panel) and imaginary part $\epsilon_2(\omega)$ (lower panel) of the dielectric function are shown at 300 K. In the inset the interband region is plotted in an expanded scale.

B. Infrared phonons

Figure 4 (upper panel) shows the temperature dependence of the reflectance spectrum in the far-infrared region. The dominant features are the four infrared-active phonons at 138, 173, 339, and 512 cm^{-1}. An assignment has already been done by Tajima *et al.*[8,9] A comparison with that study shows good agreement, with only a slightly smaller reflectance for the highest phonon mode in our measurement. $Sr_2CuO_2Cl_2$ has seven infrared phonon modes, like all the

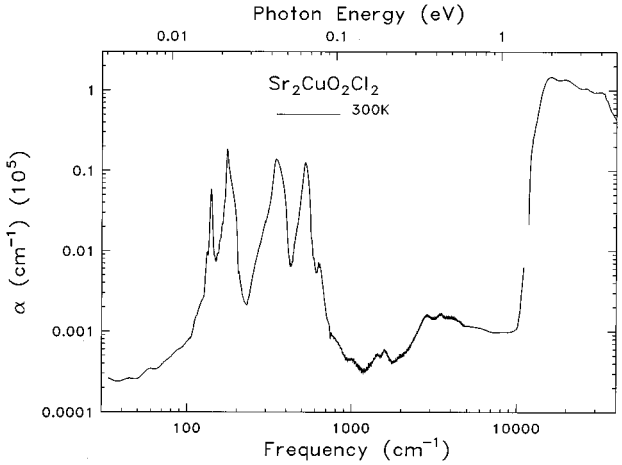

FIG. 3. The 300 K absorption coefficient $\alpha(\omega)$ versus frequency.

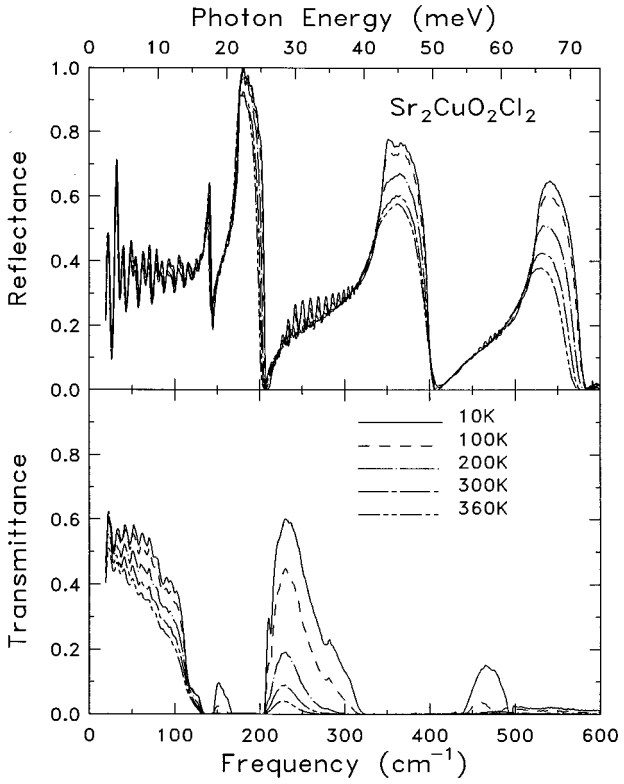

FIG. 4. The reflectance ($\mathscr{R}$) (upper panel) and transmittance spectra ($\mathscr{T}$) (lower panel) of a 100 μm thick $Sr_2CuO_2Cl_2$ sample at different temperatures.

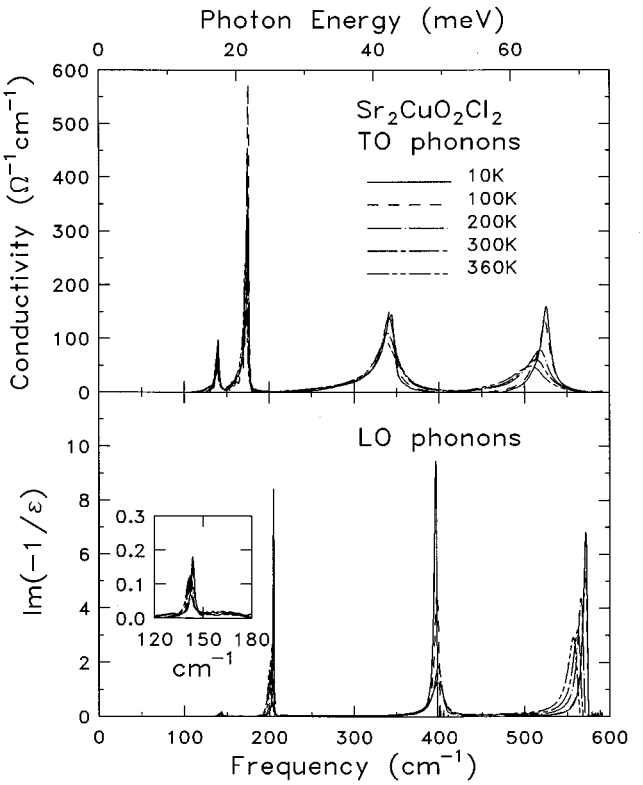

FIG. 5. Optical conductivity $\sigma_1(\omega)$ (upper panel) and loss function $\mathrm{Im}[-1/\tilde{\epsilon}(\omega)]$ (lower panel) are shown for various temperatures. The peaks correspond closely to the TO- and LO-phonon frequencies, respectively. The inset shows the lowest LO-phonon mode in more detail.

tetragonal compounds with the D_{4h}^{17} structure.[24] There are four E_u modes, with in-plane excitation, and three A_{2u} modes, with out-of-plane excitation. All four in-plane modes are seen in Fig. 4 (upper panel). On account of the different masses of oxygen and chlorine, the assignment of the modes is clear. Chlorine replaces the apical oxygen and its heavier mass causes the two lower-lying vibrations. The 140 cm^{-1} mode is an apical bending mode of the chlorine against the Cu-O unit. The 173 cm^{-1} mode is a translational vibration of the Sr-atom layer against the whole octahedron. The 339 cm^{-1} mode is a Cu-O bending mode, which modulates the bond angle, whereas the 512 cm^{-1} vibration is a Cu-O stretching mode, i.e., a bond distance modulation. The phonon features give increased reflectance with decreasing temperature. In addition, the 173 and 512 cm^{-1} modes show a hardening at lower temperatures. Finally, the 339 cm^{-1} mode splits at lower temperatures.

The lower panel in Fig. 4 shows the transmittance spectra for the same temperatures. In regions of strong absorption the transmittance vanishes. At lower temperatures the phonons sharpen and the sample becomes more transparent between them as well as below the 138 cm^{-1} mode, where the low-frequency transmittance of this insulating sample is relatively high, up to 50–60 %. The additional modulation of the spectra in regions of weak absorption is due to fringes.

The upper panel of Fig. 5 shows the real part of the optical conductivity $\sigma_1(\omega)$ and the lower panel the Im $[-1/\tilde{\epsilon}(\omega)]$, both from Kramers-Kronig analysis of the single-bounce reflectance. The peaks in $\sigma_1(\omega)$ give the TO phonon frequencies while those in $\mathrm{Im}[-1/\tilde{\epsilon}(\omega)]$ give the LO-phonon frequencies.

To do a detailed study of the phonon processes, we used a set of Lorentzian oscillators (N), which we fitted to the conductivity spectra $\sigma_1(\omega)$ at different temperatures:

$$\sigma_1(\omega)=\sum_{j=1}^{N}\frac{\omega^2\epsilon_0\omega_{pj}^2\gamma_j}{(\omega_{Tj}^2-\omega^2)^2+\omega^2\gamma_j^2}, \tag{8}$$

with ω_{pj} the oscillator strength, ω_{Tj} the eigenfrequency, and γ_j the linewidth of the jth oscillator. These parameters were used to calculate $R_s(\omega)$ using a suitable ϵ_∞ for the higher-frequency contributions above the main phonon frequencies, and gave good agreement with the measurement in the phonon region. A fit to the whole reflectance spectrum is not reasonable as long as the weak absorption features in the gap are not observed in the reflectance spectra. The parameters are presented in Table I.

Note that we were able to fit the 339 cm^{-1} vibration with a single Lorentzian oscillator at higher temperatures; however, the 10 K, 100 K, and 200 K line shapes require the use of two oscillators. We attribute the splitting of the bond angle modulation mode to a tiny distortion in the Cu-O planes below the Néel temperature. Reports on crossover effects in the material demonstrate a small XY anisotropy,[19–21] which might be related to a deviation from tetragonal symmetry. That this distortion affects only the bending mode would explain why it has not been seen in neutron measurements of J.

TABLE I. Phonon parameters from a Lorentzian fit to the FIR conductivity (reflectivity), $E\|a$.

	$T=10$ K	$T=100$ K	$T=200$ K	$T=300$ K	$T=360$ K
ω_{p1} (cm^{-1})	124	126	129	126	135.5
ω_{T1} (cm^{-1})	140	140	139	138	137.5
γ_1 (cm^{-1})	2.5	2.8	3.4	4.5	5.5
ω_{p2} (cm^{-1})	240	268.5	273	267	263
ω_{T2} (cm^{-1})	175	175	174	173	171.5
γ_2 (cm^{-1})	2.5	2	3	4.5	5
ω_{p3} (cm^{-1})	320	326	270		
ω_{T3} (cm^{-1})	333.5	334	333.5		
γ_3 (cm^{-1})	27.5	28	44		
ω_{p4} (cm^{-1})	230	270	335	422	441
ω_{T4} (cm^{-1})	343	343	341	339.5	336
γ_4 (cm^{-1})	9.5	11	16.5	27	35.5
ω_{p5} (cm^{-1})	365	375	365	410	330
ω_{T5} (cm^{-1})	525	524	518	512	507
γ_5 (cm^{-1})	14	18	29	33	38
ϵ_∞	3.8	3.8	3.8	3.8	3.8

The temperature dependence of phonon frequencies is relatively modest. The lowest-lying branch shows no temperature dependence. All other modes show a softening with increasing temperatures by up to 3% over the temperature range, with the biggest shift for the 512 cm^{-1} vibration. The analysis of the eigenfrequencies of the LO-phonon modes, estimated from the maximum position of the loss function shown in Fig. 5, reveals a similar behavior. Whereas the lower phonon modes shift within 4 cm^{-1} between 10 K and 360 K, the Cu-O stretching mode shifts about 15 cm^{-1} to lower frequency with increasing temperature.

Most of the temperature dependence can be attributed to thermal expansion. Neutron diffraction measurements show an increase of the a axis with increasing temperatures.[17] In Fig. 6 we plot both the TO-phonon frequencies (solid lines) and the LO-phonon frequencies (dashed lines) of all four modes as a function of the lattice parameter a, interpolating the $a(T)$ from Miller *et al.*[17] to find the corresponding $T(a)$. The upper scale shows the temperature dependence. In the case of the bending LO-phonon mode the TO splitting is neglected. The figure shows the strongest effect is that the Cu-O stretching mode increases in eigenfrequency with the shortening of the lattice constant a. Having no change in the atomic mass of the mode this means that the Cu-O force constant is increased by the a-axis contraction. This effect was observed by Herr *et al.*[12] investigating the phonon frequencies of single-layer cuprates in the T phase with different rare-earth substitutions. Tajima *et al.*[9] discussed the Cu-O stretching and bending TO modes for various single-layer materials. They also found that the Cu-O stretching (bond distance modulation) mode is strongly dependent on the lattice constant a, whereas the bending (bond angle modulation) mode is nearly independent of a.

C. Far-infrared absorption

In Fig. 7 we report the conductivity function below the lowest main phonon vibration, calculated from $\mathscr{R}(\omega)$ and $\mathscr{T}(\omega)$. The temperature dependence is mainly due to the changes in the transmittance. Over much of the range, the conductivity decreases at lower temperatures. At 110 cm^{-1} (13 meV) a small gap opens at lower temperatures. The energy is too high for an assignment as a zone-center spin wave gap, which can be optically allowed by anisotropy effects, and is reported in La_2CuO_4 at $\sim$1.5 meV and $\sim$2.5 meV, respectively.[25,26]

D. Midinfrared states in the gap

In this section we discuss features between the highest main phonon mode and the charge-transfer gap. In this range the reflectance is flat (Fig. 1) and hardly affected by changes in temperature. In contrast the transmittance shows sharp features with a definite temperature dependence. As mentioned above these features in the transmittance spectrum are governed by the absorption index k. For 300 K in the range between 1000 and 8000 cm^{-1} we have $10^{-3} < k < 10^{-1}$. The single-bounce reflectivity numerically calculated from $\mathscr{R}(\omega)$ and $\mathscr{T}(\omega)$ gives us a nearly flat refractive index $n \approx 1.9$. So the assumption $n \gg k$ is a reasonable approximation and an almost temperature-independent n can be assumed. Figure 8 shows $\sigma_1(\omega)$ obtained from the analysis of $\mathscr{R}(\omega)$ and $\mathscr{T}(\omega)$ described above. As the temperature is reduced, the structure at 2800 cm^{-1} sharpens and the low-frequency tail of the band edge, where there is a steep increase in $\sigma_1(\omega)$, shifts to higher frequencies. Note that the overall conductivity in this region is about two to four orders of magnitude lower than it is either in the phonon region or above the charge-transfer gap (see the lower panel of Fig. 1).

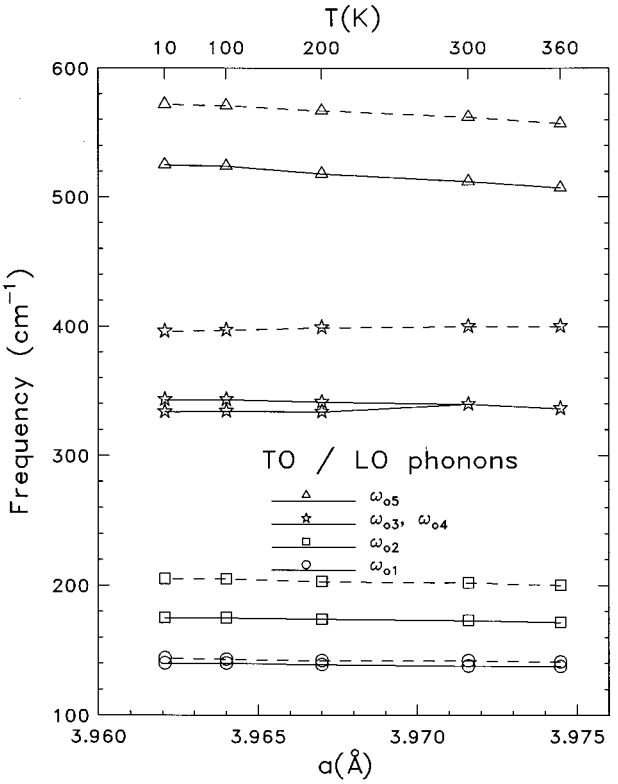

FIG. 6. The TO-phonon (solid lines) and LO-phonon frequencies (dashed lines) are plotted as a function of the lattice constant a. The upper scale shows the corresponding temperatures. The notation identifies the phonon modes and is the same as in Table I.

The high-energy wing of the 512 cm^{-1} vibration shows several satellites, at eigenfrequencies which are in a region where a finite two-phonon density of states can be expected. Thus they can be assigned as multiphonon processes. Up to now there are no data on the A_{1g}, A_{2u}, E_g, and B_{2u} modes in $Sr_2CuO_2Cl_2$ available, so that a calculation of multiphonon frequencies is not possible. A comparison with the isostructural compound La_2CuO_4, in which these modes are known up to 700 cm^{-1},[24] justifies the assumption of a multiphonon region up to 1200 cm^{-1}.

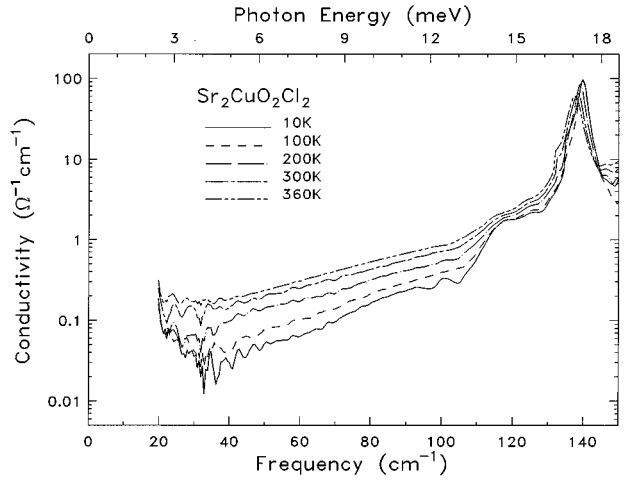

FIG. 7. Temperature dependence of the conductivity $\sigma_1(\omega)$ in the far infrared.

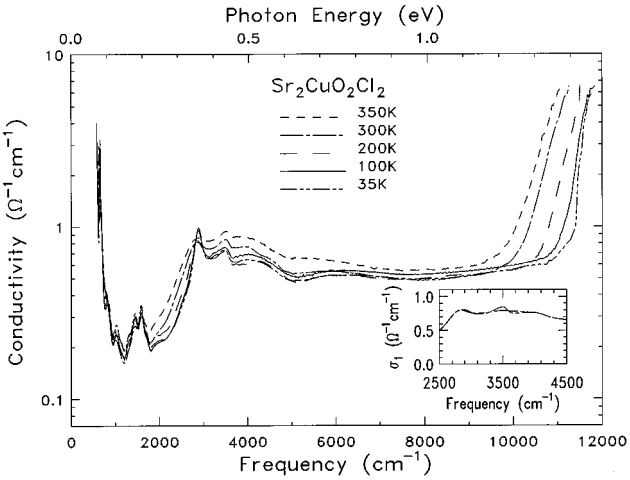

FIG. 8. Optical conductivity function $\sigma_1(\omega)$ at frequencies between the highest main phonon frequency and the charge-transfer gap for various temperatures. The inset shows the 300 K spectrum for two different samples.

The structure around 650 cm^{-1} clearly splits in two features at lower temperatures. The other features at 1000, 1430, and 1600 cm^{-1} show no distinct temperature dependence. The 1430 and 1600 cm^{-1} structures show considerable changes in strength from sample to sample, indicating perhaps that this absorption is not intrinsic to the material. Around 1350 and 1800 cm^{-1} are strong absorption bands of water. As long as the 1430 and 1600 cm^{-1} features vary so much from sample to sample and the chlorine in the material favors a contamination, these two structures might be a surface effect. The same is true of the feature at 3500 cm^{-1}, which also is characteristic of H_2O. The inset in Fig. 8 shows spectra for two different samples. From sample to sample we can see changes, which imply that this structure is also not intrinsic. In addition, there is nearly no temperature dependence of the eigenfrequency and linewidth of this feature.

More interesting are the absorption peaks above 2000 cm^{-1}, which appear to be intrinsic features in insulating cuprates. These features were first observed by Perkins *et al.*[13] in $Sr_2CuO_2Cl_2$, Nd_2CuO_4, Pr_2CuO_4, and La_2CuO_4. They also appear in $YBa_2Cu_3O_6$ and $PrBa_2Cu_3O_6$.[15] Similar results are also reported in the cupric oxide (CuO) semiconductor[14] and in La_2NiO_4.[16] Figure 9 shows a comparison of the optical conductivity $\sigma_1(\omega)$ at two temperatures with the room-temperature Raman spectrum of Tokura *et al.*[7] The Raman data have been scaled to get an overlapping plot. The two spectra agree within 10 cm^{-1} in energy of their maxima; the Raman spectrum is somewhat broader than the main infrared peak but does not show the sidebands at higher energies.

It is believed that this absorption is related to the antiferromagnetism in these materials. The energy of the first, sharpest peak corresponds closely to the two-magnon energy as seen in the Raman measurements.[7,27–30] The two-magnon energy is $\sim 2.7J$, reduced from the simple $3J$ expected (be-

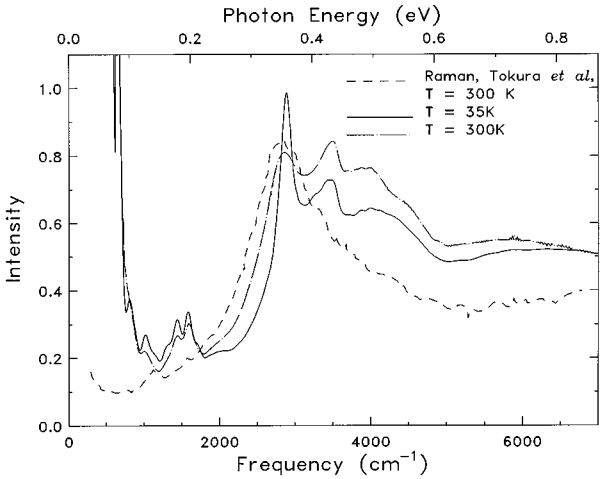

FIG. 9. A comparison of $\sigma_1(\omega)$ at 35 K and 300 K with the Raman spectrum, measured by Tokura *et al.* (Ref. 7), at 300 K. The Raman intensity is scaled to get an overlying plot.

cause six bonds are broken by flipping two neighboring spins) on account of a strong magnon-magnon interaction.[31,32] However, the interpretation of the structure in the infrared spectra is complicated by several factors. First, unlike Raman scattering, the direct two-magnon absorption is not infrared allowed in a tetragonal structure. Some sort of symmetry-breaking process is required to activate the optical absorption. Several such processes have been proposed, including disorder,[13] sidebands of direct absorption processes (such as a *d-d* exciton),[13] the involvement of an optical phonon,[27] and the orthorhombic distortion plus spin-orbit coupling.[15] Thus, the infrared response is quite different from the Raman scattering; in the latter the structure around 3000 cm^{-1} in a variety of cuprates[28,29,7] can be attributed to two-magnon scattering. The exact mechanism responsible for the infrared feature is unclear at the present time. Probably disorder can be ruled out because the oscillator strength of the absorption is remarkably similar for a variety of materials with rather different numbers of defects. Also, the close agreement between the energy of the infrared feature and the two-magnon Raman scattering may be evidence against processes that require an exciton to be created. Finally, the sidebands on the infrared spectrum are separated by approximately 1000 and 3000 cm^{-1} from the main peak. These amounts correspond to $\sim J$ and $\sim 3J$, respectively, again suggesting a magnetic origin for these features.

To provide more detail of these features we present the temperature dependence of the structures at 2800, 4000, and 6400 cm^{-1}. A fit to all peaks in the gap by a sum of Lorentzian oscillators cannot be performed in a satisfying way. Therefore we fitted each structure with a broad (strongly damped) oscillator simulating the background and a second oscillator describing the line shape. We also fitted the Raman structure in the same way. Figure 10 shows the eigenfrequencies of the different peaks. The inset shows the linewidth of the 2800 cm^{-1} structure as a function of temperature. The full stars are the result for the Raman peak. The errors in the values are less than 10%.

The 2800 cm^{-1} line shows a little redshift with increasing temperature, but moves from 300 K to 350 K back to the

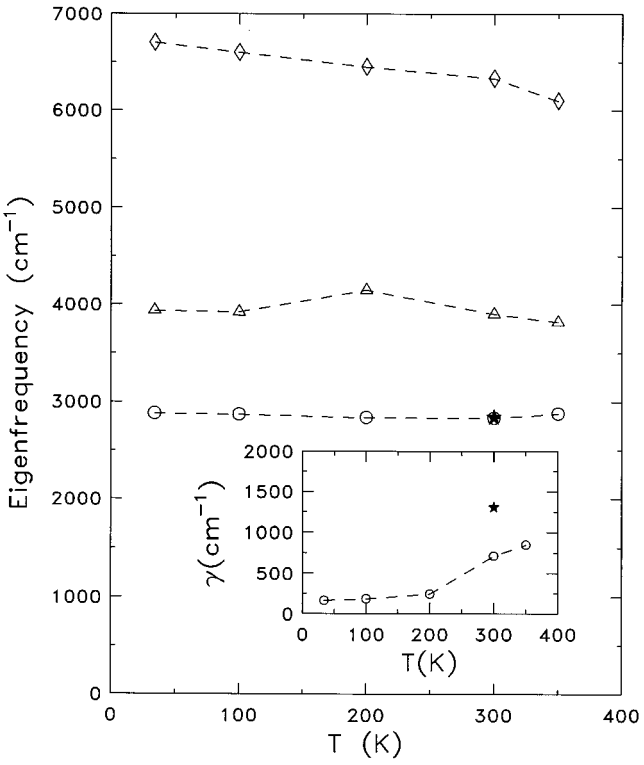

FIG. 10. Eigenfreqencies of the 2800, 4000, and 6400 cm^{-1} features versus temperature. The inset shows the linewidth of the 2800 cm^{-1} structure as a function of temperature. The full star shows the results for the fit to the Raman line at 300 K.

initial position at the lowest temperature. The 4000 cm^{-1} feature has a nonmonotonic shift to lower frequency with increasing temperature. However, the 6400 cm^{-1} feature clearly shows a redshift with increasing temperature. The strongest effect in linewidth can be seen for the 2800 cm^{-1} structure. The line broadens for temperatures higher than the Néel temperature. There is a change by a factor of $\sim$ 3 between 200 K and 300 K. The other two peaks at higher

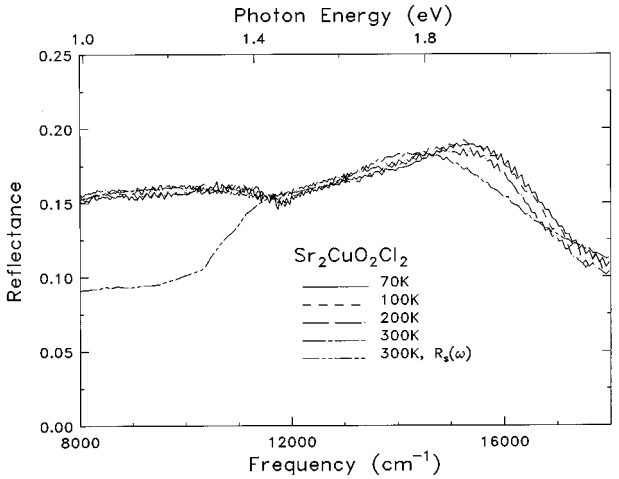

FIG. 11. Reflectance $\mathscr{R}(\omega)$ versus frequency in the region of the charge-transfer gap for different temperatures. The single-bounce reflectance $R_s(\omega)$ at 300 K is also shown.

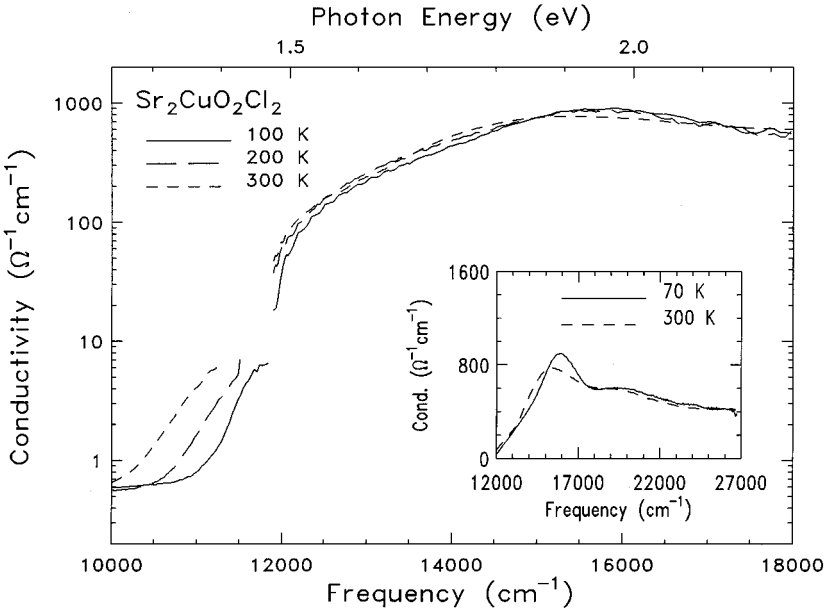

FIG. 12. Optical conductivity $\sigma_1(\omega)$ versus frequency in the region of the charge-transfer gap for selected temperatures. The lower-frequency result is obtained from $\mathscr{R}(\omega)$ and $\mathscr{T}(\omega)$. Above 12 000 cm^{-1} we used the results of Kramers-Kronig analysis. The inset shows $\sigma_1(\omega)$ in the measured high-frequency region for two temperatures 70 K and 300 K, respectively.

frequencies have nearly one order of magnitude broader linewidth. So the estimation of the eigenfrequency of these peaks is much more difficult. They reveal no significant behavior compatible to the 2800 cm^{-1} feature.

A comparison of the IR and Raman structure around 2800 cm^{-1} shows that the Raman peak is slightly shifted to higher energies (10 cm^{-1}), but 2 times broader, due to the different mechanism, although being clearly related to each other. Low-temperature Raman data of the isostructural material La_2CuO_4 show that the linewidth from the full width at half maximum is expected to sharpen only about 30% compared to room temperature.[30] In the IR data of $Sr_2CuO_2Cl_2$, this effect is much stronger, where it changes about 80%.

E. Charge-transfer gap

In Fig. 1 (lowest panel) we can see that the conductivity $\sigma_1(\omega)$ increases steeply, from 0.8 to 800 Ω^{-1} cm^{-1}, at the charge-transfer gap, which occurs around 11 000 cm^{-1}. To calculate this steep rise it is necessary to combine transmission $\mathscr{T}(\omega)$ below the gap and reflectance measurements $\mathscr{R}(\omega)$ above the gap. Figure 11 shows the temperature dependence of $\mathscr{R}(\omega)$ around the charge-transfer peak. The main effect is that the peak sharpens and moves to higher energies at lower temperatures. A similar, but stronger effect is reported by Falck *et al.*[33] in the La_2CuO_4 and Yoon *et al.*[4] in Nd_2CuO_4. We merged the reflectance data from above the gap with the extracted single-bounce reflectance (see Fig. 11) below the gap and calculated the optical properties by Kramers-Kronig analysis. Figure 12 shows the conductivity $\sigma_1(\omega)$ at three selected temperatures. The lower part, where $\sigma_1(\omega) < 10\ \Omega^{-1}\,\mathrm{cm}^{-1}$, is the result of the transmittance measurements (see Fig. 8); the upper part, where $\sigma_1(\omega) > 10\ \Omega^{-1}\,\mathrm{cm}^{-1}$, is the result of the Kramers-Kronig calculation. We have cut off the spectra where either the transmittance vanished or the single-bounce reflectance calculated from $\mathscr{R}(\omega)$ and $\mathscr{T}(\omega)$ was merged in. The procedure shows

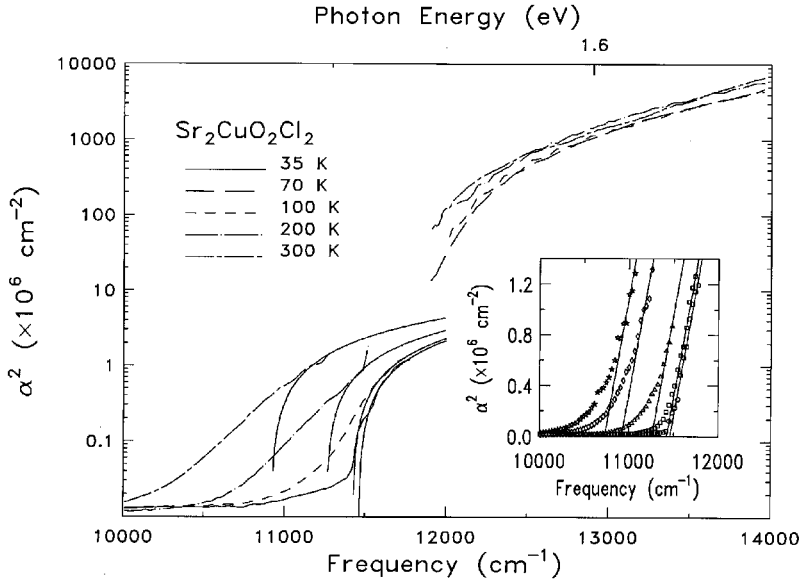

FIG. 13. $\alpha^2(\omega)$ versus frequency showing the steep increase at the band edge. The interruption is due to the change of the method of data extraction. The inset shows the strong change of $\alpha^2(\omega)$ in the low-frequency tail (circle 35 K, square 100 K, triangle 200 K, diamond 300 K, and star 350 K.) The solid lines show a fit $\alpha^2(\omega) \propto \omega - \omega_g$ to estimate the temperature dependence of the lower-lying absorption band.

a good coincidence. The missing parts could only be inserted to the curves if a measurement on a sample thinner than ~ 5 μm could be performed. The inset shows the temperature dependence on an extended scale up to 27 000 cm^{-1}. The charge-transfer peak sharpens and its maximum moves to higher energy on cooling from 300 K to 70 K.

A general approach to analyze the fundamental absorption edge is the power-law behavior of $\alpha(\omega)$ in the vicinity of the band edge. Because the insulating cuprates are strongly correlated systems, the quantum number **q** is not good and an assumption of a direct gap is reasonable. For a direct transition the form $\alpha^2(\omega) \propto \omega - \omega_g$ generally holds. Therefore we plotted in Fig. 13 the square of the absorption index, i.e. $\alpha^2(\omega)$, for different temperatures. Note the logarithmic abscissa. Again, the interruption is due to the change in the data extraction method. In the low-frequency region we clearly see a step indicating the start of strong absorption. The 35 K and 100 K data show that the steep increase moves into a plateau. So a straight connection between the two sets of curves cannot be done. We interpret this behavior as due to an additional absorption process in the low-frequency tail of the absorption edge. For example, a similar behavior can be found in semiconductors due to impurity absorption.[34] However, there are reports from Raman and absorption data of features just below the charge-transfer gap, indicating that they might be due to either intra-atomic excitations of Cu, such as *d-d* transitions, or interatomic excitations of Cu and O, such as *d-p* charge transfer.[35,13] We fitted a linear curve $\alpha_T^2(\omega) = A[\omega - \omega_g(T)]$ with constant $A = 4000$ cm^{-1} to describe the steep increase and its change in temperature. The fit is shown on a linear scale in the inset of Fig. 13. At higher temperatures the step in $\alpha^2(\omega)$ is washed out, probably due to thermal fluctuations, which increase also the uncertainty in the estimate of the fit parameters. We can see from our fit that this describes only the low-lying absorption band in the tail. The Kramers-Kronig result shows that the charge-transfer energy also increases at lower temperatures, but as long we do not have the exact curvature of $\alpha(\omega)$ in the whole range between 10 000 and 14 000 cm^{-1} we cannot do a quantitative estimation of the charge-transfer gap energy itself.

The result for $\omega_g(T)$, from the weak absorption data, is shown in Fig. 14 (upper panel, open circles). The figure also shows this energy as a function of the lattice constant a (lower panel). As described above, we used again the temperature dependence $a(T)$ given by Miller *et al.*[17] and estimated for each $\omega_g(T)$ the $T(a)$. Above 100 K the energy clearly depends linearly on the change of the lattice parameter, suggesting, that the temperature dependence of the tail absorption is mainly due to dilatation of the lattice.

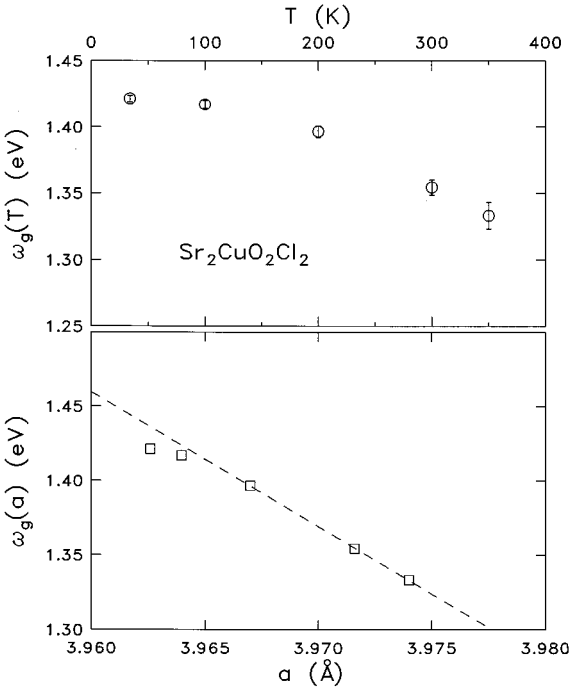

FIG. 14. Temperature dependence of ω_g in the low-frequency tail of the band edge (upper panel). The open circles show the data obtained from the changes in $\alpha^2(\omega)$. The lower panel shows ω_g versus the lattice constant a.

IV. SUMMARY

We reported reflectance and transmittance measurements of single-crystal $Sr_2CuO_2Cl_2$ between the far-infrared and the ultraviolet. The most interesting result is the midgap absorption seen in the 2000–6000 cm^{-1} range, which probably is magnetic in origin. From the phonon measurements we can see a splitting of the Cu-O bending mode at temperatures below 200 K. The Cu-O stretching mode shifts to higher frequencies at lower temperatures, indicating an increased force constant by a-axis contraction. Both reflectance and transmittance reveal a sharp increase of the conductivity at the charge-transfer gap by four orders of magnitude. There is also an additional absorption process in the low-frequency tail of the fundamental absorption edge, which has a temperature dependence mainly due to dilatation effects of the lattice.

ACKNOWLEDGMENT

The research was supported by NSF Grant No. DMR–9403894.

[1] S. Uchida, T. Ido, H. Takagi, T. Arima, Y. Tokura, and S. Tajima, Phys. Rev. B **43**, 7942 (1991).

[2] S.L. Cooper, D. Reznik, A. Kotz, M.A. Karlow, R. Liu, M.V. Klein, W.C. Lee, J. Giapintzakis and D.M. Ginsberg, B.W. Veal, and A.P. Paulikas, Phys. Rev. B **47**, 7942 (1993).

[3] A. Zibold, K. Widder, H.P. Geserich, G. Bräuchle, H. Claus, H.v. Löhneysen, N. Nücker, A. Erb, and G. Müller-Vogt, Physica C **212**, 365 (1993).

[4] Y.-D. Yoon, D.B. Tanner, B.H. O, and J. Markert (unpublished).

[5] G.A. Thomas, D.H. Rapkine, S.L. Cooper, S.-W. Cheong, L.F. Schneemeyer, and J.V. Waszczak, Phys. Rev. B **45**, 7942 (1992).

[6] Y. Tokura, H. Takagi, T. Arima, S. Koshihara, T. Ido, S. Ishibashi, and S. Uchida, Physica C **162-164**, 1231 (1989).
[7] Y. Tokura, S. Koshihara, T. Arima, H. Takagi, S. Ishibashi, T. Ido, and S. Uchida, Phys. Rev. B **41**, 11657 (1990).
[8] S. Tajima, S. Uchida, S. Ishibashi, T. Ido, H. Takagi, T. Arima, and Y. Tokura, Physica C **168**, 117 (1990).
[9] S. Tajima, T. Ido, S. Ishibashi, T. Itoh, H. Eisaki, Y. Mizuo, T. Arima, H. Takagi, and S. Uchida, Phys. Rev. B **43**, 10 496 (1991).
[10] S. Tajima, H. Ishii, T. Nakahashi, S. Uchida, M. Seki, S. Suga, Y. Hidaka, M. Suzuki, T. Murakami, K. Oka, and H. Unoki, J. Opt. Soc. Am. B **6**, 475 (1989).
[11] T. Arima, K. Kikuchi, M. Kasuya, S. Koshihara, Y. Tokura, T. Ido, and S. Uchida, Phys. Rev. B **44**, 917 (1991).
[12] S.L. Herr, K. Kamaras, D.B. Tanner, S.-W. Cheong, G.R. Stewart, and Z. Fisk, Phys. Rev. B **43**, 7847 (1991).
[13] J.D. Perkins, J.M. Graybeal, M.A. Kastner, R.J. Birgeneau, J.P. Falck, and M. Greven, Phys. Rev. Lett. **71**, 1621 (1993).
[14] F. Marabelli and G.B. Parravicini, Physica B **199 & 200**, 255 (1994).
[15] M. Grüninger, J. Münzel, A. Gaymann, A. Zibold, and H.P. Geserich (unpublished).
[16] J.D. Perkins, D.S. Kleinberg, M.A. Kastner, R.J. Birgeneau, Y. Endoh, K. Yamada, and S. Hosoya, Phys. Rev. B **52**, R9863 (1995).
[17] L.L. Miller, X.L. Wang, S.X. Wang, C. Stassis, D.C. Johnston, J. Faber, Jr., and C.-K. Loong, Phys. Rev. B **41**, 1921 (1990).
[18] D. Vaknin, S.K. Sinha, C. Stassis, L.L. Miller, and D.C. Johnston, Phys. Rev. B **41**, 1926 (1990).
[19] F. Borsa, M. Corti, T. Goto, A. Rigamonti, D.C. Johnston, and F.C. Chou, Phys. Rev. B **45**, 5756 (1992); B.J. Suh, F. Borsa, L.L. Miller, M. Corti, D.C. Johnston, and D.R. Torgeson, Phys. Rev. Lett. **75**, 2212 (1995).
[20] M. Greven, R.J. Birgeneau, Y. Endoh, M.A. Kastner, B. Keimer, M. Matsuda, G. Shirane, and T.R. Thursten, Phys. Rev. Lett. **72**, 1096 (1994).
[21] H.Q. Ding, Phys. Rev. Lett. **68**, 1927 (1992).
[22] E.E. Bell, Infrared Phys. **6**, 57-74 (1966); E.E. Russell, Ph.D. thesis, The Ohio State University, 1966.
[23] M. Tinkham, in *Far-infrared Properties of Solids*, edited by S.S. Mitra and S. Nudelman (Plenum, New York, 1970), p. 223.
[24] For a review, see R. Feile, Physica C **159**, 1 (1989).
[25] R.T. Collins, Z. Schlesinger, M.W. Shafer, and T.R. McGuire, Phys. Rev. B **37**, 5817 (1988).
[26] C.J. Peters, R.J. Birgeneau, M.A. Kastner, H. Yoshizawa, Y. Endoh, J. Tranquada, G. Shirane, Y. Hidaka, M. Oda, M. Suzuki, and T. Murakami, Phys. Rev. B **37**, 9761 (1988).
[27] J. Lorenzana and G.A. Sawatzky, Phys. Rev. Lett. **74**, 1621 (1995).
[28] K.B. Lyons, P.A. Fleury, J.P. Remeika, A.S. Cooper, and T.J. Negran, Phys. Rev. B **37**, 2353 (1988).
[29] K.B. Lyons, P.A. Fleury, L.F. Schneemeyer, and J.V. Waszczak, Phys. Rev. Lett. **60**, 732 (1988).
[30] S. Sugai, Solid State Commun. **75**, 795 (1990).
[31] R.J. Elliott and M.F. Thorpe, J. Phys. C **2**, 1630 (1969).
[32] J.B. Parkinson, J. Phys. C **2**, 2012 (1969).
[33] J.P. Falck, A. Levy, M.A. Kastner, and R.J. Birgeneau, Phys. Rev. Lett. **69**, 1109 (1992).
[34] E.J. Johnson and H.Y. Fan, Phys. Rev. **139**, 1991 (1965).
[35] R. Liu, D. Salamon, M.V. Klein, S.L. Cooper, W.C. Lee, S.-W. Cheong, and D.M. Ginsberg, Phys. Rev. Lett. **71**, 3709 (1993).